nature geoscience

ARTICLES

https://doi.org/10.1038/s41561-018-0287-1

Mode of slip and crust–mantle interaction at oceanic transform faults

Václav M. Kuna[1*], John L. Nábělek[1*] and Jochen Braunmiller[2]

Oceanic transform faults, connecting offset mid-ocean spreading centres, rupture quasi-periodically in earthquakes up to about magnitude *M* 7.0 that are often preceded by foreshocks. In addition to seismic slip, a large portion of slip takes place as aseismic creep, which likely influences initiation of large earthquakes. Although oceanic transform faults are one of the major types of plate boundaries, the exact mode of slip and interaction between the seismic and aseismic motion remains unclear. Here we present a detailed model of the mode of slip at oceanic transform faults based on data acquired from a recent temporary deployment of ocean-bottom seismometers at the Blanco Transform Fault and existing regional and teleseismic observations. In the model, the crustal part of the fault is brittle and fully seismically coupled, while the fault in the mantle, shallower than the depth of the 600 °C isotherm, creeps partially and episodically. The creep activates small asperities in the mantle that produce seismic swarms. Both mantle and the crustal zones release most of the plate-motion strain during large-magnitude earthquakes. Large earthquakes appear to be preceded by a brief episode of shallow mantle creep, accompanied by seismic swarms, which explains the observation of foreshocks and shows that mantle creep likely influences initiation of large seismic events.

The Blanco Transform Fault (BTF) is a 350-km-long oceanic transform fault (OTF) in the northeast Pacific composed of several segments with distinct morphology and seismological characteristics[1,2] (Fig. 1). Here we focus on the Blanco Ridge (BR), an east–south–east trending, prominent 130-km-long linear segment, which, compared with other segments, exhibits much higher seismic coupling[1]. Two distinct asperities along the BR appear to rupture quasi-periodically approximately every 14 years with earthquakes of moment magnitude $6.0 < M_w < 6.5$ (ref. [3]). The western asperity, centred near 128° W, was active in 1981, 1994 and 2008 with M_w 6.3–6.4 events, while the eastern asperity at 127.7° W hosted M_w 6.0–6.4 events in 1985 and 2000 (ref. [3]). A 10-km-long, geometrically and bathymetrically anomalous zone separates the two asperities (Supplementary Fig. 1).

Seismicity of the BR segment of the BTF

We deployed 55 ocean-bottom seismometers (OBS) along the full length of the BTF from September 2012 to October 2013. The experiment, enabled by recent advances in long-term OBS deployments, is only the second major project targeting an OTF[4]. Using P-wave travel times determined by first arrival picks and waveform cross-correlation, we located over 1,600 earthquakes at the BR (Fig. 1 and velocity model in Supplementary Table 1) of local magnitude (ML) 0.8–5.5. The catalogue is complete for all ML ≥ 2 events, thus lowering the earthquake detection limit by more than two orders of magnitude compared with regional and global catalogues[1]. Seismicity is abundant both in the crust and in the lithospheric mantle reaching depths of up to 13 km (Fig. 2 and Supplementary Fig. 2). Thermal modelling without and with incorporated hydrothermal cooling[5] predicts the depth limit of OTF seismicity—the 600 °C isotherm[6]—in the centre of the BR to be at 9 km and 10 km depth, respectively. Seismicity exceeds these depths along most of the BR suggesting a greater role of hydrothermal cooling than assumed in thermal modelling.

The fault geometry changes from the western to the eastern BR. West of 127.92° W (Fig. 2b, cross-sections (1)–(4)), seismicity is consistent with a vertical fault cutting the lithosphere. East of 127.92° W, mantle seismicity is offset by about 1 km southward from crustal earthquakes (Fig. 2b, cross-sections (5)–(7)). The area of the geometry change coincides with the eastern edge of the western repeating earthquake rupture patch and appears to act as a barrier between the two patches. The barrier area (Fig. 2, section (5)) also has significantly less bathymetric relief than the adjacent asperities (Supplementary Fig. 1). The barrier ruptured on 30 January 2013 in a ML 5.5 earthquake, the largest event in our catalogue. The event was followed by a one-day aftershock sequence of 37 events; all of which occurred in the barrier area.

The seismicity peaks between 3 and 7 km depth in the crust and between 8 and 13 km in the mantle. A quiet zone just below the Moho at 7 to 8 km depth separates the two regions. The fault seismicity in the crust is concentrated in the central part of the BR, between 128.2° W and 127.6° W (Fig. 2a). In contrast, fault seismicity in the lithospheric mantle stretches along the entire BR and occurs in clearly separated clusters (Supplementary Fig. 3a). All 5 recorded events with ML > 4.5 occurred in the crust. Analysis of the frequency–magnitude distribution via the Gutenberg–Richter (see Methods) law indicates a lower b value for the crust ($b = 0.78 \pm 10$) than the mantle ($b = 1.13 \pm 0.15$) (Supplementary Fig. 3c). The low b value indicates that the crustal seismicity is enhanced in larger earthquakes compared with the mantle where small events dominate. Analysis of earthquake stress drops reveals no significant differences between the crustal and mantle catalogues (Supplementary Fig. 3b). Earthquake clustering, lack of ML > 4.5 earthquakes and a higher b value suggest that mantle earthquakes rupture small brittle asperities up to about 1 km in diameter embedded in material that behaves aseismically during the period between large earthquakes.

Crustal seismicity is characterized by mainshock–aftershock sequences superimposed on the stochastic background seismicity (Supplementary Fig. 3d,e). In contrast, most events in the mantle portion of the fault occur in swarms, which are events clustered both in time and space without an initial dominant event (Fig. 3a,c

[1]College of Earth, Ocean, and Atmospheric Sciences, Oregon State University, Corvallis, OR, USA. [2]School of Geosciences, University of South Florida, Tampa, FL, USA. *e-mail: kunav@oregonstate.edu; nabelek@coas.oregonstate.edu

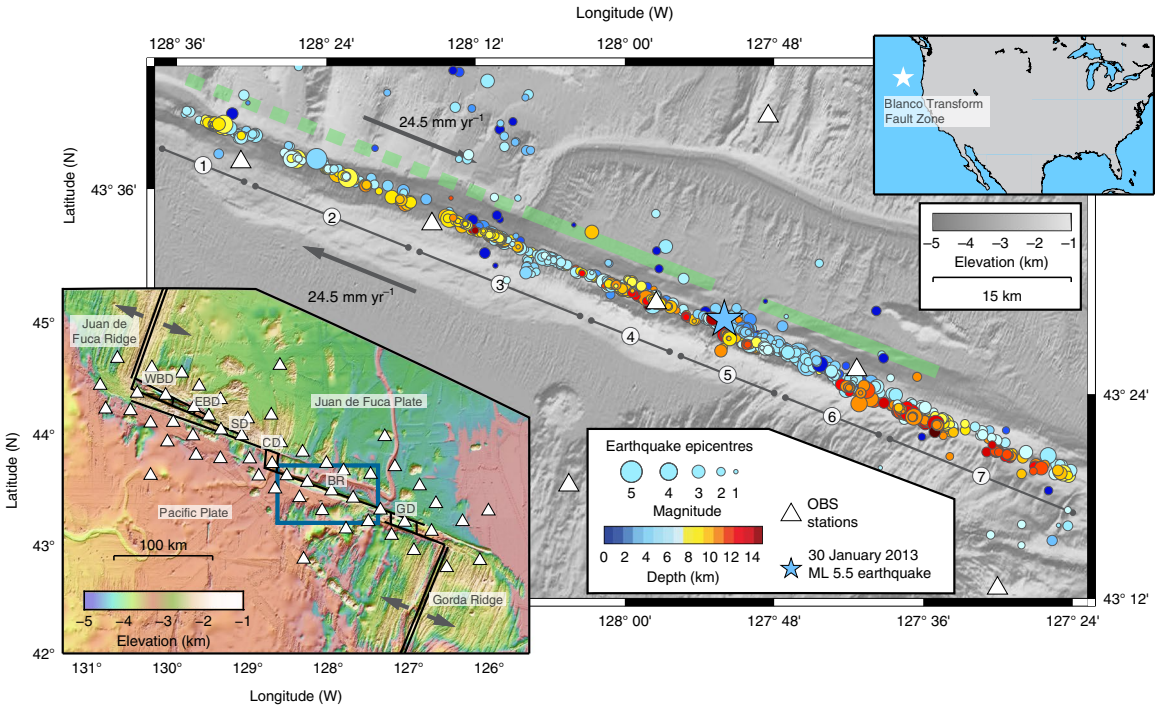

Fig. 1 | Bathymetric map of the BR with locations of earthquake epicentres and OBS stations. Cross-section segments displayed in Fig. 2 are shown by solid black lines (1)–(7). Solid green swaths indicate repeating earthquake patches based on the slip centroid[3] and the dashed green swath shows the extension of the western patch inferred from the 1994 M_w 6.4 earthquake aftershock distribution[15]. Orientation map on the lower left shows tectonics of the BTF. Bathymetric depressions are, from west to east, West Blanco (WBD), East Blanco (EBD), Surveyor (SD), Cascadia (CD) and Gorda (GD); BR refers to Blanco Ridge, the focus of this study.

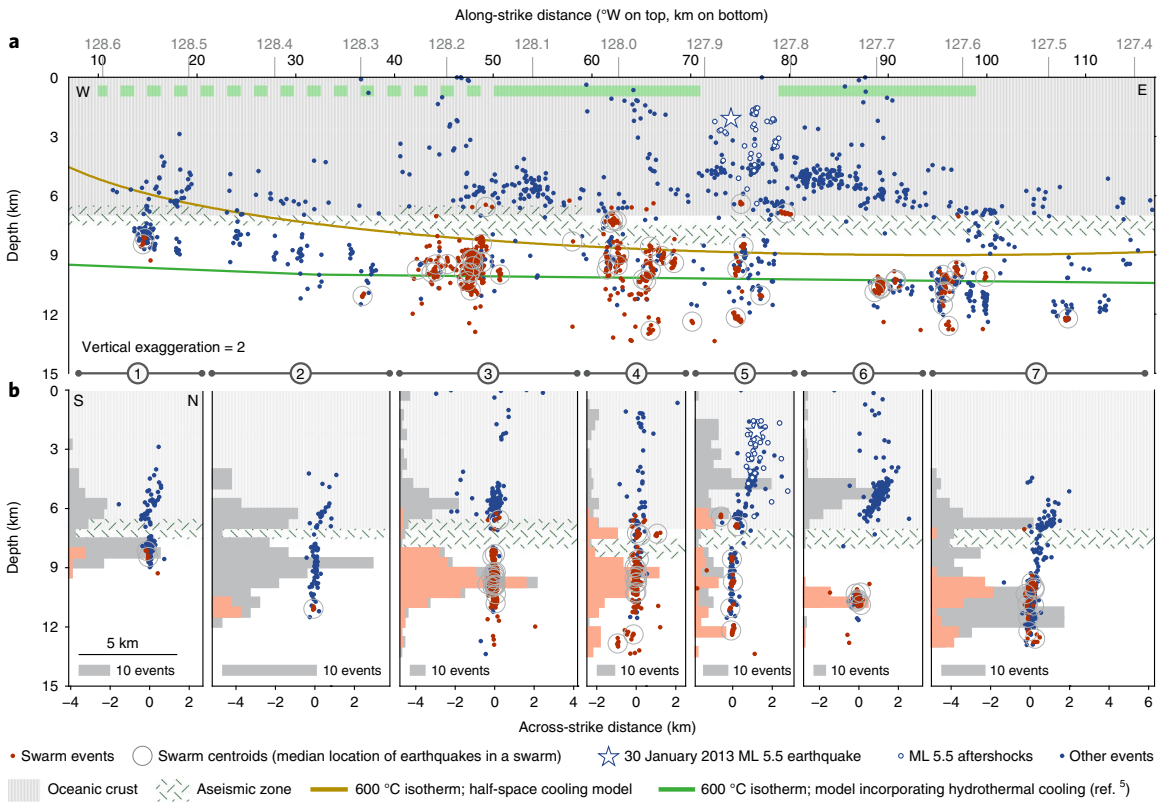

Fig. 2 | Seismicity of the BR. a, Along-strike view. Spatially, mantle earthquakes occur in small clusters. The central part of the BR (cross-sections (3)–(6)) shows frequent seismic swarms. Conversely, the flanks of the BR (cross-sections (1), (2) and (7)) show clustered events with large temporal separation. The thermal models are based on the tectonic slip rate of 56 mm yr^{-1} (ref. [25]). Using a slower plate velocity, 49 mm yr^{-1} (ref. [26]), would shift the 600 °C isotherm by about 1 km deeper. **b**, Across-strike view. Each cross-section displays the along-strike interval below, which is plotted. Histograms show swarm events in red, others in grey.

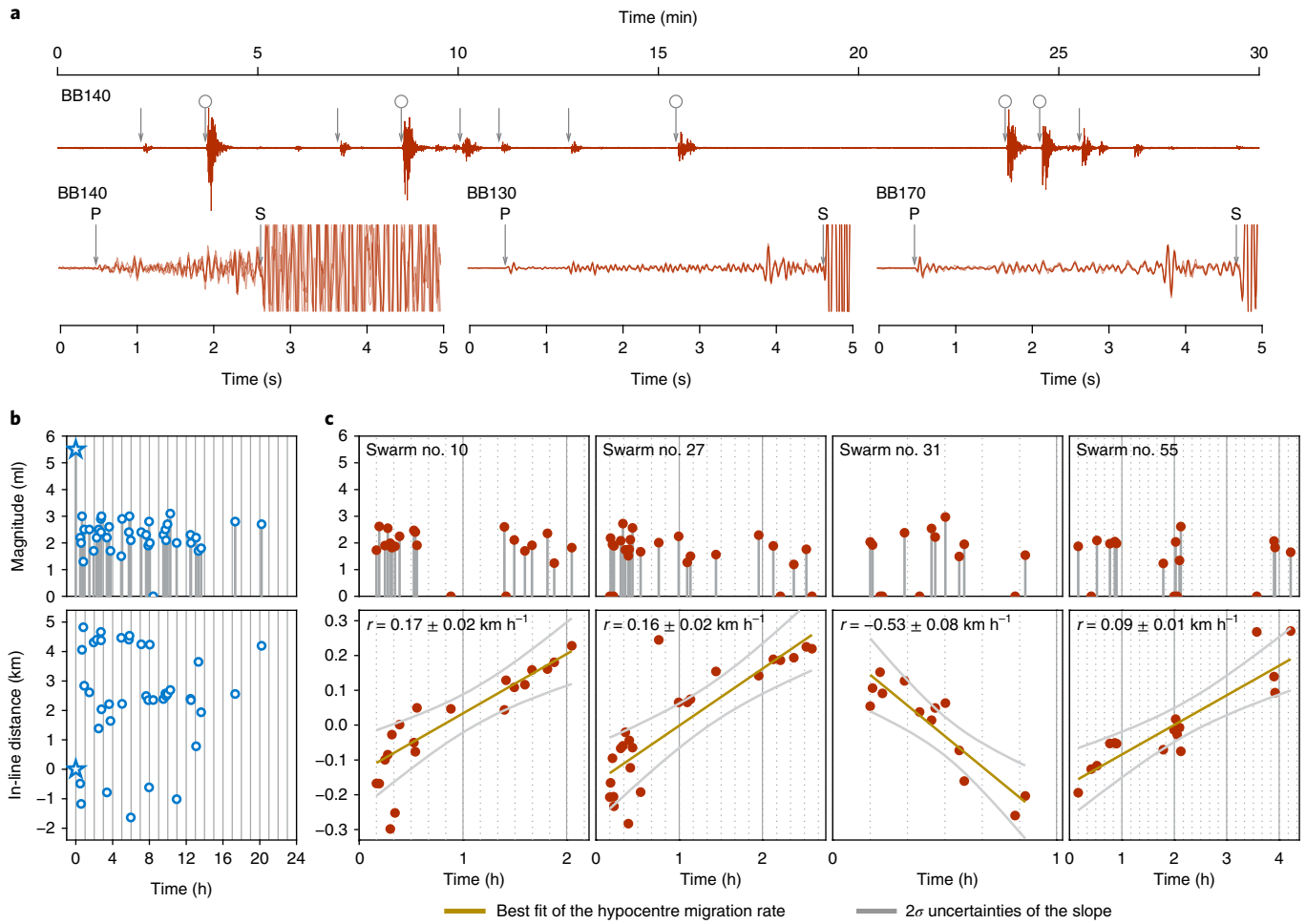

Fig. 3 | Mantle swarms versus crustal aftershock sequences. a, Selected waveforms from the 31 December 2012 seismic swarm. Top shows the first 30 minutes containing 11 events, indicated by grey arrows. For the five largest events (indicated by circles), we show normalized vertical seismograms recorded at three broadband stations BB140, BB130 and BB170 (Supplementary Fig. 2 for locations) overlain on each other. Station BB140, located on the BR, is nodal for P waves for strike-slip earthquakes, stations BB130 and BB170 are anti-nodal. **b**, Time versus magnitude (top) and time versus distance along the strike of the BR (bottom) diagrams showing the aftershock sequence after the 30 January ML 5.5 earthquake (indicated by the blue star). **c**, Same diagrams as in **b** are displayed for four selected mantle swarms. Positive rates represent eastward migration, negative westward. Distances are relative to the median location of swarm events.

and Supplementary Figs. 3–6). Almost identical waveforms of swarm events within individual swarms indicate a small source area and similar focal mechanisms (Fig. 3a). We found 58 several-hours-long swarms composed of 3 to 44 events, 40% of which have 10 or more events (see Supplementary Table 2 for details). Unlike events in crustal aftershock sequences, which are distributed stochastically with no migration in time, swarm events migrate along the strike of the BR (Fig. 3b,c). The observed hypocentre migration rates for 24 BR swarms range from about 100 to 2,000 m h^{-1} with a median value of 370 m h^{-1} (Supplementary Fig. 6). Studies of the San Andreas Fault in California associated seismic swarms with geodetically observed creep and found that the propagation speed of the creep events agrees with the hypocentre migration speed within swarms[7,8]. The hypocentre migration rates of creep-triggered swarms in both continental and oceanic transform fault environments were found to be on the order of 100–1,000 m h^{-1} (Fig. 3c)[7,9], which is consistent with velocities observed at the BR. We thus infer that the swarms observed in the mantle portion of the fault occur in direct response to aseismic fault creep.

The presence of aseismic creep at depths shallower than the 600 °C isotherm in the mantle portion of an OTF can be attributed to a change in peridotite rheology from velocity-weakening to velocity-strengthening frictional mode[10]. Serpentinization of peridotite, predominantly present as antigorite and chrysotile under BR conditions (Supplementary Fig. 7), offers a plausible explanation for the rheology change as fractured and highly permeable rocks at OTFs provide a natural pathway for water circulation[11]. Serpentinite behaves in a velocity-strengthening frictional mode at low, tectonic slip rates and transforms to a velocity-weakening mode at high, earthquake-induced slip rates[12,13]. Thus, the fault in the mantle may release a portion of the tectonically accumulated slip aseismically as creep and the rest during large BR earthquakes.

Mantle serpentinization and seismic coupling of the fault

To assess the importance of these slip modes, we quantify the apparent seismic coupling of the mantle portion of the fault from the centroid depth of 6.5 km for the 1994 M_w 6.4 earthquake[1] (see Methods for details). We assume the earthquake ruptured the fault from the ocean floor down to 13 km depth and released all accumulated strain. The resulting apparent seismic coupling suggests that about 40% of the mantle slip occurs during large seismic events. The absence of large earthquakes purely in the mantle indicates

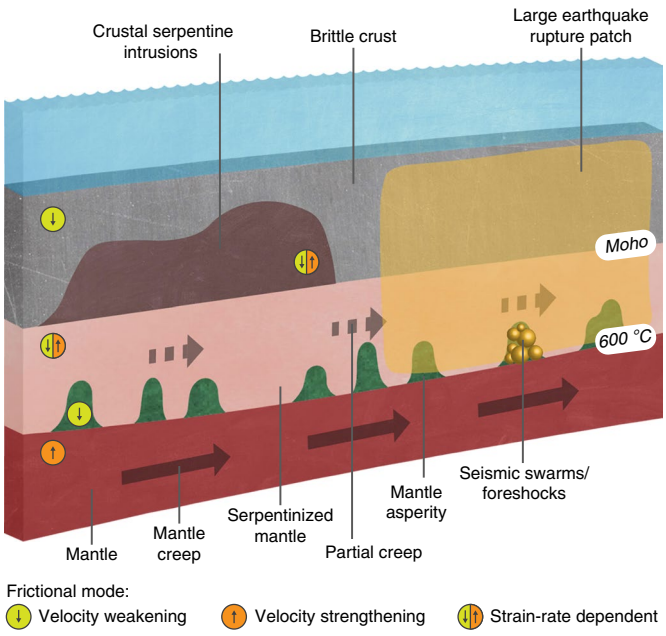

Fig. 4 | Mode of slip of the BR transform fault. The fully seismically coupled fault in the brittle crust (grey) is loaded from beneath by partial, episodic creep on the fault in the serpentinized mantle (pink) above the 600 °C isotherm. The creep in the mantle activates small asperities (green) that release energy primarily in seismic swarms (yellow spheres). In a situation where an episode of creep shortly precedes a large-magnitude earthquake (yellow patch), swarms appear as foreshocks of the large earthquake. Apparent seismic coupling in the crust may vary laterally due to serpentinite intrusions (deep purple) from the mantle. The fault in the mantle lithosphere beneath the 600 °C isotherm is fully creeping at the tectonic rate and loads the upper parts of the fault.

that most of the remaining 60% is released via aseismic creep. We suggest that the mantle asperities generating the earthquake swarms during the inter-seismic period are either dry peridotite patches out of reach of water circulation, or a product of dehydration of antigorite and its transition back to olivine at temperatures near 520 °C (ref. [14]). The above seismic coupling in the mantle is for a fully seismically coupled crust. This is supported by the estimated rupture length of the M_w 6.4 earthquake, which is about 20 km for a fully coupled crust (see Methods), and is similar to an independent estimate[3]. The brittle character of the crust is supported by Omori-style seismicity distributed over the entire crust width.

The BR is unique from the other segments of the BTF with its higher seismic coupling[1]. Lower coupling on the other segments likely results from variable fluid circulation in the lithosphere and intrusion of serpentinite into the crust[4,15]. Thus averaged over the entire BTF, the overall seismic coupling is much lower than along the BR. This is in broad agreement with low seismic coupling observed at many OTFs globally from teleseismic observations, which only provide averages over entire transform faults[16–18]. BTF studies (ref. [1] and here) indicate that seismic coupling on OTFs may not be uniformly low, but can vary strongly between segments.

Mode of slip and crust–mantle interactions

Based on our observations, we propose a detailed model of mode of fault slip at the BR. The model may also be applicable at other OTFs (Fig. 4), particularly at those with long, simple segments such as the BR. The crustal part of the fault is brittle, fully seismically coupled and behaves in a velocity-weakening frictional mode. Serpentinite intrusions into the crust may limit the seismic coupling in parts of the fault zone. The fault zone in the mantle shallower than the 600 °C isotherm contains serpentinized peridotite, which creeps episodically in the velocity-strengthening mode during the inter-seismic period, but slips seismically during large OTF earthquakes. Frictionally velocity-weakening asperities situated at and above the 600 °C boundary respond to the surrounding episodic creep through seismic swarms. The fault in the lithosphere beneath the 600 °C isotherm creeps freely at the tectonic rate loading the shallower parts. Our model provides a testable description of OTF slip observed on the BR, which is consistent with previous OTF studies based on local, regional and teleseismic data.

OTF earthquakes appear to have predictable behaviour. In the long-term perspective, they occur quasi-periodically[3,19,20], which probably results from steady loading of well-defined asperities that are stable over multiple seismic cycles. In the short-term perspective, they are preceded by foreshocks[21,22] and perhaps also by precursory long-period signals[23,24] (possibly representing episodic creep). We observe two foreshocks for the ML 5.5 earthquake, preceding it by 55 and 20 minutes, respectively. Both foreshocks are part of a small, 3-event swarm that occurred at 10 km depth in the mantle (Supplementary Fig. 8). We interpret the precursory foreshock sequence as a direct response to an episode of shallow mantle creep shortly before the mainshock. The shallow mantle creep is thus not only loading the fully coupled, brittle crust in a long-term perspective, but also acts as a short-term direct trigger for large OTF earthquakes.

In recent years aseismic fault motion has been observed in various tectonic environments including continental transform faults and subduction zones, generating questions about its influence on seismic slip. Although these environments differ from OTFs in many ways, we think that the key principles of the aseismic–seismic slip interaction may be similar. Studying OTFs may reveal important details of this process at much shorter timescales than for other tectonic environments, due to the combination of high slip rate and narrow seismogenic zone. We believe our model provides a framework for future OTF studies as well as improves our understanding of processes that lead to earthquake generation.

Online content

Any methods, additional references, Nature Research reporting summaries, source data, statements of data availability and associated accession codes are available at https://doi.org/10.1038/s41561-018-0287-1.

Received: 23 March 2018; Accepted: 5 December 2018;
Published online: 21 January 2019

References

1. Braunmiller, J. & Nábělek, J. Segmentation of the Blanco Transform Fault Zone from earthquake analysis: complex tectonics of an oceanic transform fault. *J. Geophys. Res. Solid Earth* **113**, B07108 (2008).
2. Embley, R. W. & Wilson, D. S. Morphology of the Blanco Transform Fault Zone-NE Pacific: implications for its tectonic evolution. *Mar. Geophys. Res.* **14**, 25–45 (1992).
3. Boettcher, M. S. & McGuire, J. J. Scaling relations for seismic cycles on mid-ocean ridge transform faults. *Geophys. Res. Lett.* **36**, L21301 (2009).
4. McGuire, J. J. et al. Variations in earthquake rupture properties along the Gofar transform fault, East Pacific Rise. *Nat. Geosci.* **5**, 336–341 (2012).
5. Roland, E., Behn, M. D. & Hirth, G. Thermal-mechanical behavior of oceanic transform faults: implications for the spatial distribution of seismicity. *Geochem. Geophys. Geosyst.* **11**, Q07001 (2010).
6. Boettcher, M. S., Hirth, G. & Evans, B. Olivine friction at the base of oceanic seismogenic zones. *J. Geophys. Res. Solid Earth* **112**, B01205 (2007).
7. Lohman, R. B. & McGuire, J. J. Earthquake swarms driven by aseismic creep in the Salton Trough, California. *J. Geophys. Res. Solid Earth* **112**, B04405 (2007).
8. Linde, A. T., Gladwin, M. T., Johnston, M. J. S., Gwyther, R. L. & Bilham, R. G. A slow earthquake sequence on the San Andreas fault. *Nature* **383**, 65–68 (1996).

9. Roland, E. & McGuire, J. J. Earthquake swarms on transform faults. *Geophys. J. Int.* **178**, 1677–1690 (2009).
10. Scholz, C. H. *The Mechanics of Earthquakes and Faulting* (Cambridge Univ. Press, Cambridge, 1990).
11. Francis, T. Serpentinization faults and their role in the tectonics of slow spreading ridges. *J. Geophys. Res. Solid Earth* **86**, 11616–11622 (1981).
12. Kohli, A. H., Goldsby, D. L., Hirth, G. & Tullis, T. Flash weakening of serpentinite at near-seismic slip rates. *J. Geophys. Res. Solid Earth* **116**, B03202 (2011).
13. Reinen, L. A. Seismic and aseismic slip indicators in serpentinite gouge. *Geology* **28**, 135–138 (2000).
14. Guillot, S., Schwartz, S., Reynard, B., Agard, P. & Prigent, C. Tectonic significance of serpentinites. *Tectonophysics* **646**, 1–19 (2015).
15. Dziak, R. P. et al. Recent tectonics of the Blanco Ridge, eastern Blanco Transform Fault Zone. *Mar. Geophys. Res.* **21**, 423–450 (2000).
16. Boettcher, M. S. & Jordan, T. H. Earthquake scaling relations for mid-ocean ridge transform faults. *J. Geophys. Res. Solid Earth* **109**, B12302 (2004).
17. Okal, E. A. & Langenhorst, A. R. Seismic properties of the Eltanin Transform System, South Pacific. *Phys. Earth Planet. Interiors* **119**, 185–208 (2000).
18. Bird, P., Kagan, Y. Y. & Jackson, D. D. in *Plate Boundary Zones* (eds Stein, S. S. & Freymueller, J. T.) 203–218 (AGU, Washington DC, 2002).
19. McGuire, J. J. Seismic cycles and earthquake predictability on East Pacific Rise transform faults. *Bull. Seismol. Soc. Am.* **98**, 1067–1084 (2008).
20. Sykes, L. R. & Ekström, G. Earthquakes along Eltanin transform system, SE Pacific Ocean: fault segments characterized by strong and poor seismic coupling and implications for long-term earthquake prediction. *Geophys. J. Int.* **188**, 421–434 (2012).
21. McGuire, J. J. Immediate foreshock sequences of oceanic transform earthquakes on the East Pacific Rise. *Bull. Seismol. Soc. Am.* **93**, 948–952 (2003).
22. McGuire, J. J., Boettcher, M. S. & Jordan, T. H. Foreshock sequences and short-term earthquake predictability on East Pacific Rise transform faults. *Nature* **434**, 457–461 (2005).
23. McGuire, J. J., Ihmle, P. F. & Jordan, T. H. Time-domain observations of a slow precursor to the 1994 Romanche transform earthquake. *Science* **274**, 82–85 (1996).
24. Abercrombie, R. E. & Ekström, G. Earthquake slip on oceanic transform faults. *Nature* **410**, 74–77 (2001).
25. Wilson, D. S. Confidence intervals for motion and deformation of the Juan de Fuca Plate. *J. Geophys. Res. Solid Earth* **98**, 16053–16071 (1993).
26. DeMets, C., Gordon, R. G. & Argus, D. F. Geologically current plate motions. *Geophys. J. Int.* **181**, 1–80 (2010).

Acknowledgements

The seismic stations for the project were provided by the Ocean Bottom Seismograph Instrument Pool (http://www.obsip.org), funded by the National Science Foundation (NSF). This research was supported by NSF grants OCE-1031858, OCE-1131767 and OCE-1737073. We thank the crews of RV *Melville* and RV *Oceanus,* OBSIP technicians and volunteers who contributed to data collection.

Author contributions

J.L.N. and J.B. designed the study and collected the dataset. V.M.K. and J.L.N. created the seismicity catalogue. V.M.K. conducted the data analysis. All authors discussed results and contributed to the manuscript.

Competing interests

The authors declare no competing interests.

Additional information

Supplementary information is available for this paper at https://doi.org/10.1038/s41561-018-0287-1.

Reprints and permissions information is available at www.nature.com/reprints.

Correspondence and requests for materials should be addressed to V.M.K. or J.L.N.

Publisher's note: Springer Nature remains neutral with regard to jurisdictional claims in published maps and institutional affiliations.

Methods

Seismic data. The Blanco Transform Fault OBS Experiment, conducted from September 2012 to October 2013, deployed 30 broadband Güralp CMG3T seismometers and 25 short-period Mark Products L-28LB seismometers co-located with Scripps Institution of Oceanography differential pressure gauges. Earthquakes were located using 100 samples-per-second data streams.

Seismicity catalogue. We constructed the earthquake catalogue from P-wave arrivals using Boulder Real Time Technologies' Antelope software. The data streams were filtered with a 4 to 15 Hz bandpass filter to enhance P-wave arrivals. The arrivals were detected by comparing short-term and long-term signal averages (STA/LTA). Detections at individual stations were associated with earthquakes using a search over a grid with 2.2 km horizontal and 2 km vertical spacing. To minimize grid search artefacts, we accepted only events with at least 10 defining P-wave arrivals. The associated events were subsequently located using a Marquardt algorithm[27]. For calculation of theoretical travel times, we used a one-dimensional P-wave velocity model based on ref. [1] with the mantle P-wave velocity decreased by 3% relative to the original model to match local travel-time observations (Supplementary Table 1).

We used only the best-recorded events. From the catalogue, we removed events missing first arrivals at 1 of the 3 closest stations, events with fewer than 6 arrivals at the 13 closest stations, and events with a station azimuthal gap larger than 110°.

Some events within seismic swarms remained undetected or did not pass the requirements for well-recorded events. We used a template-matching procedure to add them to the catalogue. In each swarm, we selected the best-constrained event and used its P-wave arrivals (1 s window starting at the P-wave arrival) for cross-correlation over the duration of the swarm. We set the limit for P-wave detection to a cross-correlation coefficient ≥0.6 and require at least 5 arrivals to define an event. The catalogue used in this study contains 1,626 earthquakes, of which 420 were constrained by template matching.

Relative relocation. For the purpose of our study, precise locations of earthquakes relative to each other are more important than their absolute locations within the lithosphere. Using the travel-time data, we relocated the catalogue with the relative location algorithm hypoDD[28]. A maximum separation distance of 10 km (approximately one half of the average inter-station distance) was used to define an event cluster and we required at least 8 arrivals at mutual stations to create an inter-event link.

Swarms were relocated individually using the relative arrival times obtained from waveform cross-correlation. All events within a swarm were relocated starting from the initial location of the best-constrained event.

Earthquake depth distribution. Along most of the BR, we see a bimodal distribution of seismicity with depth. Abundant seismicity in the crust and the mantle is separated from each other by a narrow zone with a low number of events just below the Moho (approximately 7–8 km). To show reliability of the depth distribution, we display waveforms of 11 earthquakes occurring directly (with epicentral distance <2.5 km) beneath the station BB200, which is situated on top of the BR (Supplementary Fig. 2). We align waveforms on the first P-wave arrival and show that the S–P times increase systematically from ~1 s for earthquakes at ~2 km depth to 1.8 s for earthquakes at ~9 km depth. The S-wave normal move-out corresponds to a P-wave to S-wave velocity ratio (v_p/v_s) of 1.85 and 1.73 in the crust and mantle, respectively. The S-wave arrivals also suggest a high v_p/v_s ratio of ~2.7 in the uppermost crust, suggesting highly fractured and possibly altered fault gauge. The distinct difference in S–P arrival times between earthquakes in the lower crust (~1.5 s) and in the lithospheric mantle (~1.8 s) supports the existence of a quiet zone between crustal and mantle seismicity.

Frequency–magnitude distribution. We evaluate the frequency–magnitude distribution through the Gutenberg–Richter law, $P(m)=10^{a-bm}$, where $P(m)$ is the number of events with magnitude ≥ m, for $m \geq$ magnitude of completeness. Constants a and b denote earthquake productivity and the frequency–magnitude falloff, respectively. The a and b values are obtained by least-squares regression.

Correlation integral. To show temporal distribution of events in catalogues, we use the concept of a correlation integral, which displays the distribution of seismicity over a wide range of inter-event times. The correlation integral $C(\tau)$, defined as $C(\tau)=\frac{2}{N(N-1)}\sum_{i=1}^{N-1}\sum_{j=i+1}^{N}\theta(\tau-|t_i-t_j|)$ (ref. [29]), describes temporal closeness of events relative to each other. $C(\tau)$ counts the number of event couples, defined by their origin times t_i and t_j, that are closer to each other than an inter-event time τ. Counting over all possible event pairs is done through the Heaviside function θ, which returns 1 for an inter-event time $|t_i-t_j|$ less than τ and 0 otherwise. $C(\tau)$ is normalized by the total number of event couples (N is number of events). $\log_{10}C(\tau)$ is a monotonically increasing function of $\log_{10}\tau$, which reaches its maximum when τ is larger than the largest inter-event origin-time difference in the dataset. To identify characteristic patterns in inter-event times, we use the rate of change of the correlation integral, $d(\tau)=\frac{\delta\log_{10}C(\tau)}{\delta\log_{10}\tau}$. $d(\tau)$ is large for inter-event times that occur often and small for inter-event times that occur infrequently. $d(\tau)$ is very sensitive to rate changes and a powerful tool to characterize the temporal event distribution. In addition, by replacing the inter-event time with inter-event distances, we can define the correlation integral in space and describe the distribution of a set of points in space (Supplementary Fig. 3a). Refer to ref. [29] for a detailed description on how to compute and interpret the rate of change of the correlation integral for an earthquake catalogue.

Hypocentre migration rate. We measured hypocentre migration rates along the strike of the BR. Positive velocities represent eastward migration, negative westward. The hypocentre migration rates were estimated by linear regression using a re-weighted (bi-square) least-squares approach and considered reliable for P values less than 0.05. Out of 58 swarms, 26 (46%) show migration rates ranging between 60 and 2,120 m h^{-1} with a median value of 370 m h^{-1}. Out of the 26 swarms, 21 migrate between 100 m h^{-1} and 1,500 m h^{-1} (see Supplementary Fig. 6 and Supplementary Table 2 for details). Westward migration was observed in 14 cases while 12 swarms migrate eastwards.

Earthquake stress drop. We calculated the stress drop using the Brune model[30], where the corner frequency f_c in the body wave spectrum defines the rupture radius $a=0.372\frac{v_s}{f_c}$ with v_s the shear wave velocity at the source (we use the lower-crust velocity $v_s=3.73$ km s^{-1}). To estimate the stress drop $\Delta\sigma$, we assume a circular rupture for which $M_0=\frac{16}{7}\Delta\sigma a^3$ with M_0 the seismic moment. We obtain the corner frequency f_c by least-squares fitting of P-wave spectra by the spectral response of a theoretical circular source. The seismic moment is calculated from the earthquake magnitude as $M_0=10^{\frac{3}{2}(M_w+6.033)}$ (ref. [31]), assuming $M_w=$ ML, for small events.

Apparent seismic coupling. Seismic coupling on a fault is defined as the ratio between the seismic and tectonic slip. For the calculation of the apparent seismic coupling of the mantle, we use the 1994 M_w 6.4 earthquake with a centroid depth of $C=6.5$ km (ref. [1]). The seismic moment distribution balances at the moment-release centroid, and thus, for our case with the centroid in the crust, we can write $Lu^c\sum_i\mu_i t_i c_i = Lu^c\sum_j\mu_j t_j c_j + Lu^m\sum_m\mu_m t_m c_m$, where L is the rupture length, u^c *and* u^m are the displacement during the event in the crust and mantle, respectively. μ is the rigidity, t is layer thickness and c is vertical distance between the earthquake moment-release centroid and the centre of a layer. Indexes i and j represent crustal layers, index m represents mantle layers. The left side of the equation is the moment contribution of layers above the centroid, the right side is the moment below the centroid. The rigidity μ is obtained from the S-wave velocity and density model (Supplementary Table 1). To obtain seismic coupling, we make the following reasonable assumptions: (1) the earthquake rupture extended from the ocean floor (0 km) down to the bottom limit of seismicity at 13 km, (2) the event released all accumulated strain over the inter-seismic period in the crust and the mantle; thus $u^c=u\chi^c$ and $u^m=u\chi^m$, where u is the accumulated tectonic slip and χ^c and χ^m are seismic coupling in the crust and mantle, respectively. Substituting into the expression above, we obtain $\chi^m/\chi^c=(\sum_i\mu_i t_i c_i-\sum_j\mu_j t_j c_j)/\sum_m\mu_m t_m c_m$. If the fault in the crust is fully seismically coupled ($\chi^c=1$) and using the model in Supplementary Table 1, we obtain $\chi^m=0.42$. If the crust is not fully coupled, the mantle coupling drops proportionally. For the 1994 earthquake, we can determine the length of the rupture for a fully seismically coupled crust and compare it with independent estimates. The length can be expressed as $L=M_0/(u^c\sum_i\mu_i t_i+u^c\sum_j\mu_j t_j+\chi^m u^c\sum_m\mu_m t_m)$, with M_0 the seismic moment of the earthquake, χ^m determined above and u^c equal to the tectonic loading of 49 mm yr^{-1} (ref. [26]) over the inter-seismic period of 14 yr (ref. [3]). This results in $L=19$ km, which is similar to the length shown in Fig. 2 (based on ref. [3]), and supports the assumption of a fully coupled crust in parts of the BR.

Data availability

The OBS dataset is archived at the IRIS Data Management System (http://www.iris.edu). X9 is the network code for the Plate Boundary Evolution and Physics at an Oceanic Transform Fault System project[32]; 7D is the network code for the Cascadia Initiative Community Experiment – OBS component data[33]. Raw bathymetry data, used in Fig. 1 and Supplementary Fig. 1, are available from the authors.

References

27. Pavlis, G. L., Vernon, F., Harvey, D. & Quinlan, D. The generalized earthquake-location (GENLOC) package: an earthquake-location library. *Comput. Geosci.* **30**, 1079–1091 (2004).
28. Waldhauser, F. & Ellsworth, W. L. A double-difference earthquake location algorithm: method and application to the northern Hayward Fault, California. *Bull. Seismol. Soc. Am.* **90**, 1353–1368 (2000).
29. De Rubeis, V., Loreto, V., Pietronero, L. & Tosi, P. in *Modelling Critical and Catastrophic Phenomena in Geoscience* (eds Bhattacharyya, P.& Chakrabarti, B. K.) 259–279 (Springer, Berlin Heidelberg, 2006).
30. Brune, J. N. Tectonic stress and the spectra of seismic shear waves from earthquakes. *J. Geophys. Res.* **75**, 4997–5009 (1970).
31. Hanks, T. C. & Kanamori, H. A moment magnitude scale. *J. Geophys. Res. Solid Earth* **84**, 2348–2350 (1979).
32. Nábělek, J., Braunmiller, J. Plate boundary evolution and physics at an oceanic transform fault system. *International Federation of Digital Seismograph Networks* https://doi.org/10.7914/SN/X9_2012 (2012).
33. IRIS OBSIP Cascadia Initiative Community Experiment - OBS component. *International Federation of Digital Seismograph Networks* https://doi.org/10.7914/SN/7D_2011 (2011).